



Photocatalytic and gas sensing applications of sol-gel processed GO/(Zn_xNi_{1-x})O ternary composites

Matthew D. Femi^{1,2,3} · Agnes C. Nkele^{2,4} · Michael O. Nwakanma² · Adil Alshoaibi⁵ · G. H. Jain¹ · S. D. Shinde¹ · B. A. Ezekoye² · A. B. C. Ekwealor² · S. M. Abhinay¹ · G. E. Patil¹ · Fabian I. Ezema^{2,6}

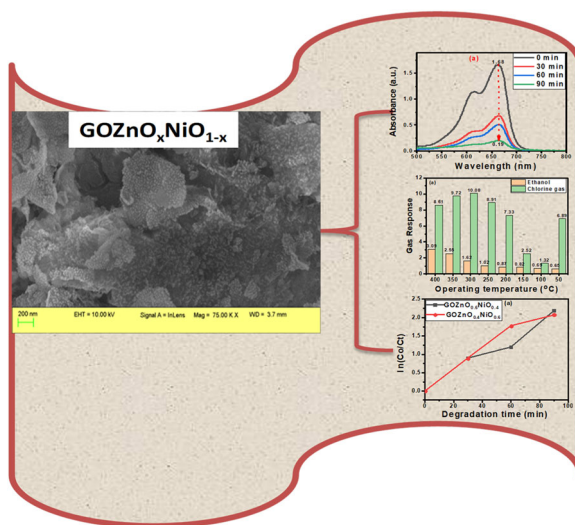
Received: 13 June 2024 / Accepted: 6 August 2024

© The Author(s), under exclusive licence to Springer Science+Business Media, LLC, part of Springer Nature 2024

Abstract

This research studies the effects of volume ratios on the properties of GO/(Zn_xNi_{1-x})O ternary composite prepared by a sol-gel technique. The ratios were produced by keeping the volume of graphene oxide, GO constant whilst varying the volumes of zinc oxide, ZnO, and nickel oxide, NiO to produce the GO/ZnO_{0.4}NiO_{0.6} and GO/ZnO_{0.6}NiO_{0.4} nanocomposites. The structural, morphological, elemental, optical, gas sensing and photocatalytic properties of the synthesized nanocomposites have been investigated. EDS results confirmed the presence of graphene oxide, nickel oxide, and zinc oxide in the composite. The band gap energy values for the GOZnO_{0.6}NiO_{0.4} and GOZnO_{0.4}NiO_{0.6} composites are 3.0 eV and 3.4 eV, respectively with high absorbance properties. The functional groups and vibrational modes belonging to carbon, oxygen, nickel, zinc were shown in the FT-IR spectra. The gas sensing properties were tested with ethanol and Cl₂ at 100 ppm and 10 V; with the highest sensitivity recorded for Cl₂. The synthesized ternary composite was highly effective in dye degradation with efficiency of over 85% and high photocatalytic activity performance. Results from the characterization showed potential application of the composites in gas sensing and photocatalytic devices.

Graphical Abstract



✉ Agnes C. Nkele
chinecherem.nkele@unn.edu.ng

¹ Department of Physics, SNJBs KKHA Arts, SMGL Commerce and SPHJ Science College, Chandwad, India

² Department of Physics & Astronomy, University of Nigeria Nsukka, Enugu, Nigeria

³ Kogi State College of Education, Ankpa, Kogi, Nigeria

⁴ Department of Physics, Colorado State University, Fort Collins, CO, USA

⁵ Department of Physics, College of Science, King Faisal University, Al Ahsa, Saudi Arabia

⁶ Africa Centre of Excellence for Sustainable Power and Energy Development (ACE-SPED), University of Nigeria, Nsukka, Enugu, Nigeria

Keywords Graphene oxide · ZnO · NiO · Ternary composites · Gas sensor · Photocatalyst

Highlights

- Sol–gel synthesis of $(\text{Zn}_x\text{Ni}_{1-x})\text{O}$ binary composites at x values of 0.4 and 0.6.
- Compact morphology with cubic and hexagonal crystal structures.
- Good thermal conductivity with energy band gap values from 3.0 eV to 3.4 eV.
- Over 85% photocatalytic efficiency was gotten over time with the composites exhibiting maximum gas sensing ability to Cl_2 gas.
- Potential applications of composites in photocatalytic and gas sensing devices.

1 Introduction

In recent years, scientists have shown great interest in preparing heterogeneous nanomaterials as a single nanocomposite [1]. Graphene oxide (GO) is a unique material that can be viewed as a single monomolecular layer of graphite with various oxygen-containing functionalities such as epoxide, carbonyl, carboxyl, and hydroxyl groups [2]. When the GO is reduced with a suitable process, the reduced graphene oxide (rGO) formed resembles graphene but contains residual oxygen and other heteroatoms, as well as structural defects [3]. GO-incorporated membranes consist of a high mechanical strength and thermal stability [4]. The emergence of nanocomposites has positively affected nanotechnology and nanoscience in different areas such as medicine, electronics, gas sensors, and photocatalytic devices [5, 6]. Metamorphosing the chemical composition of these nanostructures allows us to tune their properties and therefore generate new properties so that the nanomaterial would be more efficient [7–9]. Nano composites exhibit additional properties and activities due to the improved synergy between the physiochemical characteristic of the mono-nano components [10]. Nano composites are potentially important in various applications such as fuel cells, batteries, photovoltaic devices, UV detectors, gas sensors, photocatalytic degradation systems, and solar cells [11–13]. Various techniques such as sol–gel [14], hydrothermal [15], homogeneous coprecipitation [11], deposition precipitation [16], and impregnation [17] have been developed for the preparation of nano composites [18]. Among these techniques, sol–gel is one of the facile, simplest, and cheapest methods of preparing nano composites with relatively high specific surface area at low temperatures that give room for diverse applications [19].

Several materials have been synthesized by sol–gel technique under different deposition conditions. Nanocomposites of graphene oxide/alumina have been prepared by a dry sol–gel method by thermally decomposing the precursor in the presence of hexane [20]. The results show that the composites were able to minimize agglomeration, increase surface coverage, and enhance the porous nature of the electrodes [21, 22]. Reduced GO/Silica nanocomposites having a carbon-controlled phase were prepared in the presence of inert gas [23]. The

materials showed a crystalline structure with reduced defect density and good dispersive properties in the matrix. GO/titanium dioxide nanofilms were synthesized for photonic application by dip-coating [24]. The results showed the reduced energy band gap from 3.42 to 3.38 eV upon heat treatment, lower Raman spectra as more GO was added, and better photocatalysis after five hours. Lim et al. processed aerogels of graphene from GO to increase the electrical conduction and make the sample chemically stable [25]. The aerogels exhibited good features for large-area fabrication of electrodes with good performance. Hydroxyapatite/GO nanofilms were prepared at low temperatures by Jang, Oh, and Lee [26]. The samples were biocompatible with good crystallinity and good adhesive properties.

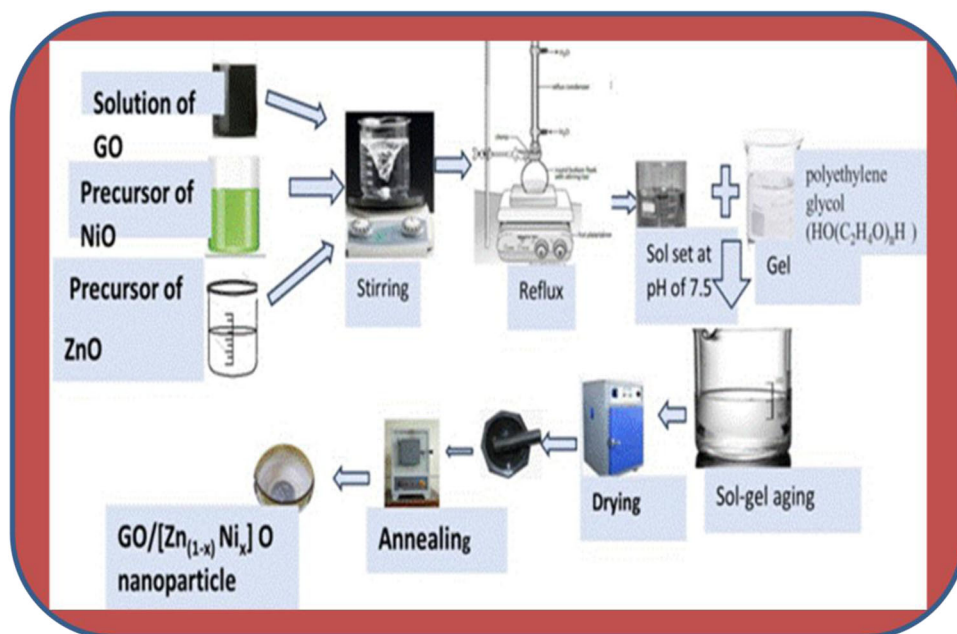
In this study, we synthesized graphene oxide by sol–gel processing technique at room temperature. The distinguishing factor from the reviews is that the volume of graphene oxide (GO) was kept constant in this work whilst varying the volume ratios of nickel and zinc by x values of 0.6 and 0.4 to yield $\text{GO}/\text{ZnO}_{0.6}\text{NiO}_{0.4}$ and $\text{GO}/\text{ZnO}_{0.4}\text{NiO}_{0.6}$ nanocomposites respectively. The synthesized ternary composites were characterized for their structural, morphological, optical, field emission, elemental, and photoluminescent features. The gas sensing and photocatalytic properties of the synthesized and characterized ternary composite have also been investigated.

2 Experimental details

2.1 Materials and method

All the analytical grade chemicals were purchased from Sigma Aldrich with 98% purity and used without further purification. The chemical reagents used were graphene oxide, zinc nitrate hexahydrate, nickel (II) acetate tetrahydrate, ethanol, ammonium hydroxide, and polyethylene glycol. Graphene oxide, GO was synthesized by sol–gel method while methanol was used to dissolve 0.1 M of GO powder in a beaker. 0.1 M each of Zinc nitrate hexahydrate and Nickel (II) acetate tetrahydrate precursors were then dissolved in ethanol and mixed to prepare

Fig. 1 Experimental flow chart of the synthesized GO ternary composites



zinc oxide and nickel oxide composites. The appropriate volume ratio of ($x=0.4$ and 0.6) for the zinc and nickel composites was mixed thoroughly at varying ratios while maintaining a constant volume of the graphene oxide. The ternary composites were refluxed by constantly stirring for 300 Rotations per hour (RPH) at a temperature of $80\text{ }^{\circ}\text{C}$ for 4 h. The solution was cooled to room temperature so that the sol would be formed. The pH of the sol was maintained at 7.5 by the drop-wise addition of ammonium hydroxide. The gel was formed by mixing 10 ml of polyethylene glycol ($\text{HO}(\text{C}_2\text{H}_4\text{O})_n\text{H}$) with 90 ml of distilled water in the ratio of 1:9, respectively. The gel formed was mixed with the sol to form the sol-gel and allowed to age for 24 h. The 24 h period will give room for the mixture to have better homogeneity, uniform distribution, and good stabilization. Washing was done on the sol-gel several times to remove supernatant liquid and extract the residue. The residue was dried in an oven at a temperature of 343 K for 8 h. The ternary composite obtained was then crushed to powder and calcinated at 673 K for 2 h. A flow chart of the experimental process has been sketched below in Fig. 1.

2.2 Characterizations

The prepared samples were characterized for their structural, morphological, elemental, optical properties, photocatalytic, and gas sensing features. The crystal structure and crystallite size of the $\text{GO}/\text{ZnO}_{0.6}\text{NiO}_{0.4}$ & $\text{GO}/\text{ZnO}_{0.4}\text{NiO}_{0.6}$ were confirmed by Japan Rigaku, Smart Lab X-ray Diffractometer (XRD) using X-ray Source Cu $\text{K}\alpha$ Model Miniflex 600 Make Rigaku. The experimental setup for the XRD analysis includes a radiation source, the sample preparation stage, instrument setup, X-ray diffraction measurement, data acquisition, and

data analysis stage. Fourier-transform infrared spectroscopy (FTIR) was performed with IR Affinity—1 having a diamond ATR Shimadzu Spectrometer and using FT-IR spectrum 2 (Perkin Elmer). The experimental setup for FTIR measurement includes Michelson interferometer, beam splitter, mirrors, sample cell, spectrum analyzer, and data detector. Absorbance plots were gotten using LAMBDA 750 (Perkin Elmer) UV-Vis-NIR Spectrophotometer. The experimental setup for UV-Vis characterization contains a light source, dispersion device like a diffraction grating, a cuvette, detector, monochromator, and data collector which aids data analysis. Field Emission Scanning Electron Microscopy (FESEM) imaging and energy dispersive X-ray spectroscopy (EDS) were performed using the Carl Zeiss Model Supra 55 Germany. The experimental setup for electron microscopy involves sample preparation, vacuum operation for taking measurements, and image analysis for unique features. The experimental setup for EDS characterization involves the excitation source, X-ray detector, pulse processor, and spectrum analyzer. The EDS detector used is of Oxford company manufacturing. Photoluminescence spectra were performed using the Fluorolog (Horiba). Photoluminescence was performed using the JASCO Spectrofluorometer Model—FP-8300 WRE, and TEM images were collected using the JEOL JEM 2100 plus. The experimental setup for PL measurement includes a laser/light source, grating monochromator, photodiode, cryostat, detector, and other optical components. The experimental setup for photocatalytic characterization involves a spectral analyzer, external four-lamp reactor, a catalyst, and reactivity accesser. The experimental setup for thermal conductivity measurement includes the sample material, heater/coolant, and temperature detector. The experimental setup for gas sensing includes the probing gas,

sample to be measured, and a sensing device. The equipment is set up in good working condition at the Department of Physics, SNJBs KKHA Arts, SMGL Commerce, and SPHJ Science College Chandwad, 423101, India.

3 Results and discussion

3.1 X-ray diffraction (XRD)

Figure 2 represents the XRD patterns of GO/ZnO_{0.4}NiO_{0.6} and GO/ZnO_{0.6}NiO_{0.4} composites respectively. The plots show crystalline patterns that have prominent peaks revealed at different 2theta angles with the GO/ZnO_{0.4}NiO_{0.6} composite exhibiting better crystallinity. The GO/ZnO_{0.4}NiO_{0.6} composite shows a cubic structure with $\alpha = \beta = \gamma = 90^\circ$ while the GO/ZnO_{0.6}NiO_{0.4} composite showed a hexagonal structure with $\alpha = \beta = 90^\circ$ and $\gamma = 120^\circ$. This phase transformation from the cubic to the hexagonal crystal structure is evidence of the effect of volume concentration variations in both composites [20]. The Miller indices labeled at the observed peaks of each composite correspond to the JCPDS numbers: 96-723-8487 and 96-710-4641 for the GO/ZnO_{0.6}NiO_{0.4} and GO/ZnO_{0.4}NiO_{0.6} composites respectively. At 2theta angle values of 31.8°, 34.4°, 36.4°, 43.3°, 63.1°, 72.8°, 74.8°, 77.1°, and 79.2°; the composites recorded hkl indices of (100), (002), (003), (102), (110), (105), (113), (202), and (006) respectively. The indices obtained at 31.8° and 43.3° belong to the graphene oxide component; the 34.4°, 36.4°, and 63.1° indices belong to the zinc oxide component; while the rest of the indices belong to the nickel oxide constituent. The most prominent peak belonging to the (003) lattice plane was obtained at a 2theta angle value of 36.1°. It can be observed that the intensity and number of prominent peaks increased as the volume of NiO

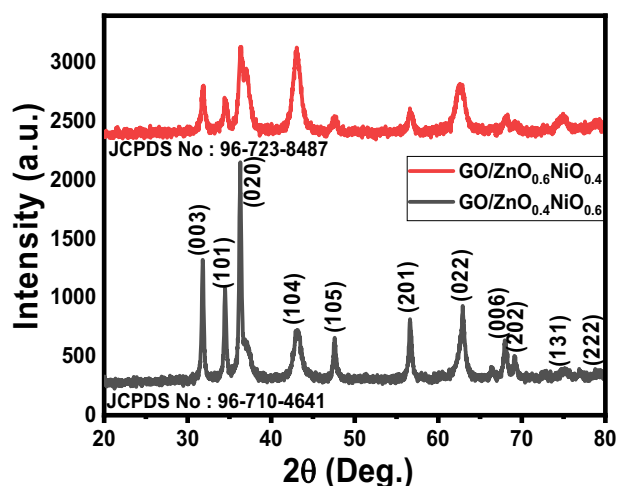


Fig. 2 X-ray diffraction plots of the synthesized GO/ZnO_{0.6}NiO_{0.4} and GO/ZnO_{0.4}NiO_{0.6} composites

increased from 0.4 to 0.6 in the ternary composites while the noise level in the plots can be seen to reduce as the volume of ZnO was reduced. Overall, the X-ray diffraction plots of the ternary composites exhibited good crystallinity with slight variations in their structural features owing to their different material compositions [27].

Williamson–Hall (W-H) theory was useful in determining the crystallite size and microstrain of the composites using the equation $\beta \cos \theta = 4\epsilon \sin \theta + \frac{k\lambda}{D}$ in a plot of $\beta \cos \theta$ against $4\sin \theta$ [28, 29]. The gradient calculated gave the estimated values of the microstrain (ϵ) as 0.195 and 0.453 for the GO/ZnO_{0.6}NiO_{0.4} and GO/ZnO_{0.4}NiO_{0.6} composites respectively. The crystallite size, D obtained for the GO/ZnO_{0.6}NiO_{0.4} and GO/ZnO_{0.4}NiO_{0.6} composites were calculated from Scherrer's equation [30] as 13.35 and 11.30 nm respectively. The dislocation density (δ) which was calculated using the formula $\delta = 1/D^2$ [31] yielded 0.0056 (nm)⁻² and 0.0078 (nm)⁻² values respectively for the GO/ZnO_{0.6}NiO_{0.4} and GO/ZnO_{0.4}NiO_{0.6} composites. The variations observed in the peak intensities, crystallite sizes, micro strains, and dislocation densities of the ternary composites may be attributed to the changes in the volume ratio of the ZnO and NiO materials in the composite [32].

3.2 Electron microscopy study

The electron micrographs of the composites synthesized at various volume ratios were analyzed using scanning electron microscopy (SEM) and transmission electron microscopy (TEM) whose image outputs are shown in Figs. 3 and 4 respectively. The SEM micrographs in Fig. 3 were taken at a magnification of 200 k and show compact nanopebbles that are densely accumulated over the surface. The GO/ZnO_{0.6}NiO_{0.4} micrograph showed interlocked agglomerates while the GO/ZnO_{0.4}NiO_{0.6} composite gave flake-like agglomerates with reduced interlock. The effects associated with changing the volume of zinc oxide can be seen as slight cracks due to the induced stress at increased volume while a decrease in the volume gave rise to a brighter contrast free of agglomeration [33]. The differentials observed in the dense morphologies are as a result of variations in the volume ratios of the ZnO and NiO constituents. This is evidence of the effects associated with varying the volume ratios of the compounds making up the ternary composites. This dense morphology is useful for photocatalytic and solar cell applications [34].

The transmission electron micrographs shown in Fig. 4 were obtained at a magnification of 50 k. The micrographs reveal web-like mesh of nanopores with good interconnectivity. The GO/ZnO_{0.6}NiO_{0.4} sample gave less dense morphology as compared to the GO/ZnO_{0.4}NiO_{0.6} sample due to the smaller volume ratio of the nickel oxide component. The budding feature of these composites decreases as the volume of the zinc oxide increases and appears as agglomerates across the surface

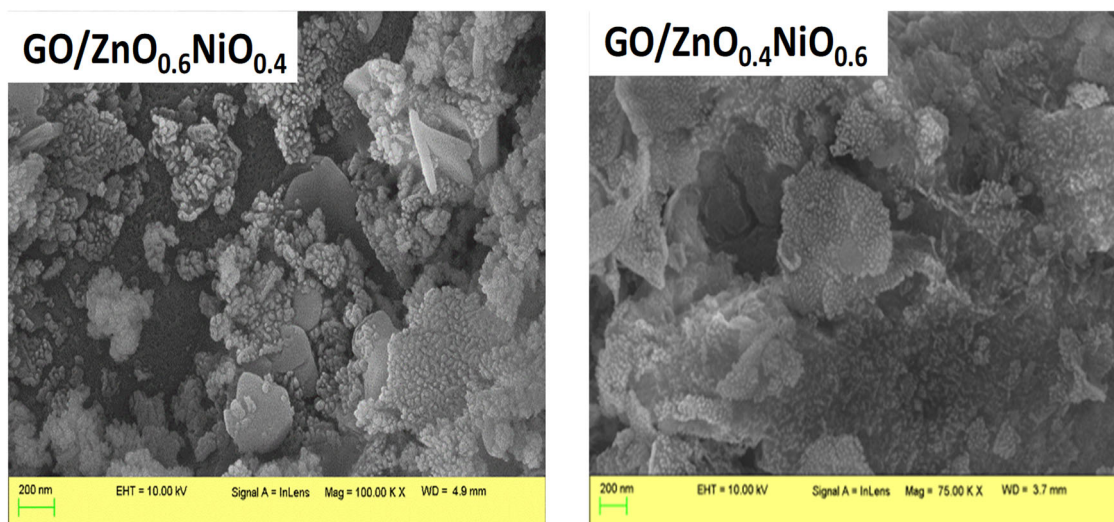


Fig. 3 SEM images of the prepared graphene oxide ternary nanocomposites

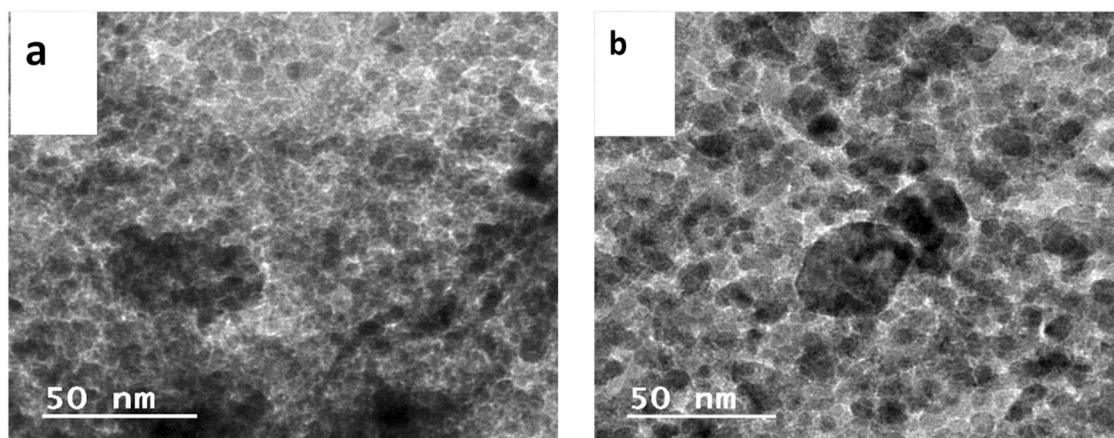


Fig. 4 TEM images of the synthesized (a) $\text{GO/ZnO}_{0.6}\text{NiO}_{0.4}$ and (b) $\text{GO/ZnO}_{0.4}\text{NiO}_{0.6}$ ternary composites

[35]. The effect of the volume ratios are evident in the non-uniform surface distribution seen in the micrographs which also reflects in their different structural build-ups [34].

3.3 EDS analysis

The elemental composition of the nano composites was estimated by the EDS technique. The EDS spectrum evidently reflects the presence of carbon (C), oxygen (O), nickel (Ni), and zinc (Zn) as shown in Fig. 5. The presence of these elements confirms the deposition of the ternary nano composites and proper synthesis of the composites. The composites synthesized at various volume ratios gave different percentages for each element. The percentage of each atom present in the $\text{GOZnO}_{0.4}\text{NiO}_{0.6}$ composite is C (11.48%), O (40.56%), Ni (29.32%), and Zn (18.63%) while the elemental composition of the $\text{GOZnO}_{0.6}\text{NiO}_{0.4}$ ternary composite is C (9.59%), O (42.79%), Ni (9.04%) and Zn (38.58%) for. The percentage of

each element changes with the volume ratio of each constituent oxide in the composites and confirms proper synthesis in the correct proportion. The absence of other peaks shows the high purity level of the synthesized ternary composites regardless of their volume ratios [36].

3.4 Ultraviolet-visible (UV-vis) spectrophotometry

Figure 6 shows the absorbance versus wavelength plots of the $\text{GO/ZnO}_{0.6}\text{NiO}_{0.4}$ and $\text{GO/ZnO}_{0.4}\text{NiO}_{0.6}$ composites respectively. These absorbance plots have the Tauc plots seen as an inset which was useful in determining the energy band gap values of the synthesized materials. The broad humps could be due to the large surface area created by the synergy between the different composite materials. The reduced absorbance curves seen towards the visible light region could be attributed to the effect of varying the volume of the precursors during the composite formation [37]. The absorbance

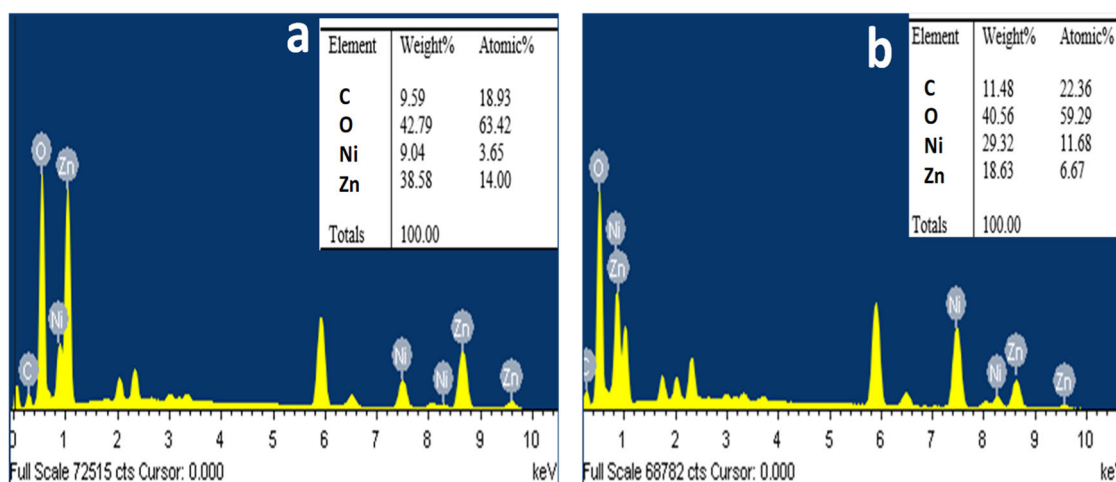


Fig. 5 Energy dispersive spectra of the (a) $\text{GO/ZnO}_{0.6}\text{NiO}_{0.4}$ and (b) $\text{GO/ZnO}_{0.4}\text{NiO}_{0.6}$ ternary composites

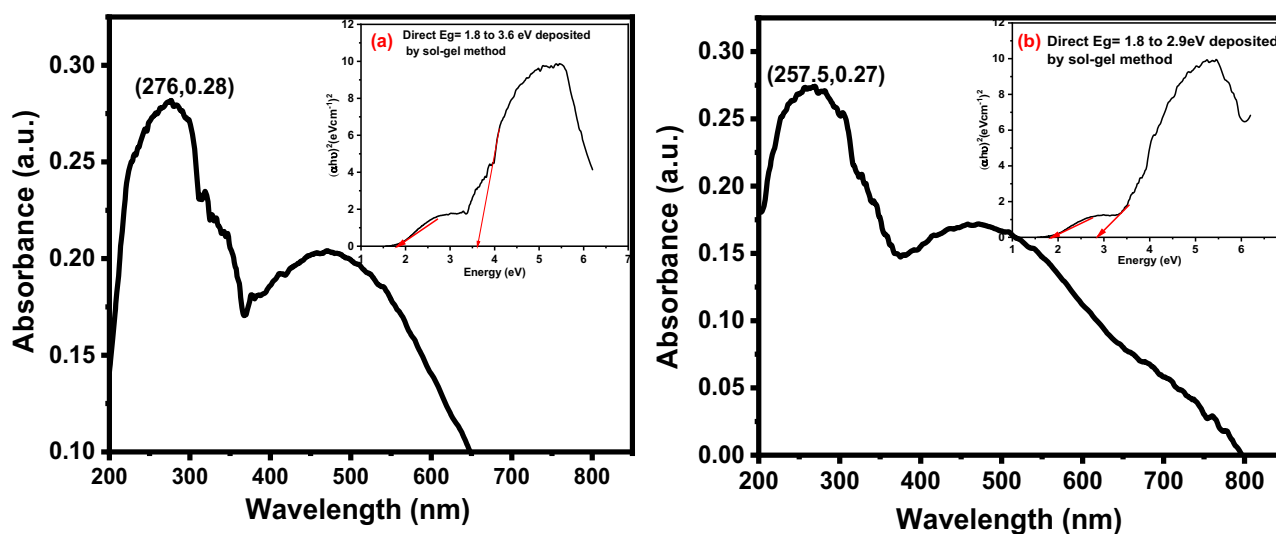


Fig. 6 Absorbance plots of the ternary (a) $\text{GO/ZnO}_{0.6}\text{NiO}_{0.4}$ and (b) $\text{GO/ZnO}_{0.4}\text{NiO}_{0.6}$ composites with the energy band gap plots attached as the insets

plots recorded maximum values of 0.28 and 0.27 respectively for the $\text{GO/ZnO}_{0.6}\text{NiO}_{0.4}$ and $\text{GO/ZnO}_{0.4}\text{NiO}_{0.6}$ composites at wavelengths of 276 nm and 257.5 nm. Their corresponding direct energy band gap values obtained (as seen in the insets) are 3.4 eV and 3.0 eV. The slightly varying energy band gap values associated with electron transfer could be due to changes in the volume ratio of the precursors. These volume changes also led to shifts in the estimated energy band gap values of the composites. It can be observed that reducing the volume of zinc oxide led to a slight decrease in their energy band gap values due to increased energetic interactions between the component atoms [38].

3.5 Photoluminescence (PL) studies

For the PL measurement, 10 mg of the nanocomposites were added to 10 ppm of methylene dye at an intensity of 80 W/

m^2 in a photocatalytic reactor. The samples were taken at an exposure time interval of 20 min for 120 min. The obtained photoluminescence (PL) spectra of the synthesized ternary composites at different volume ratios were recorded in the wavelength region from 200 to 800 nm as shown in Fig. 7. The different color emissions are shown to represent different PL intensities attained by the composites at different wavelengths within the ultraviolet and visible electromagnetic spectra. The $\text{GO/ZnO}_{0.4}\text{NiO}_{0.6}$ composite recorded more PL counts than the $\text{GO/ZnO}_{0.6}\text{NiO}_{0.4}$ sample in the near-visible spectrum. The differentials exhibited by the ternary composites in their PL intensities can be attributed to the variational composition which led to a reduction in the PL intensity at higher wavelength regions [39]. The variations in the volume ratios of the zinc oxide and nickel oxide constituents also contributed to slight peak shifts in the observed spectra. It can be observed that as the volume of

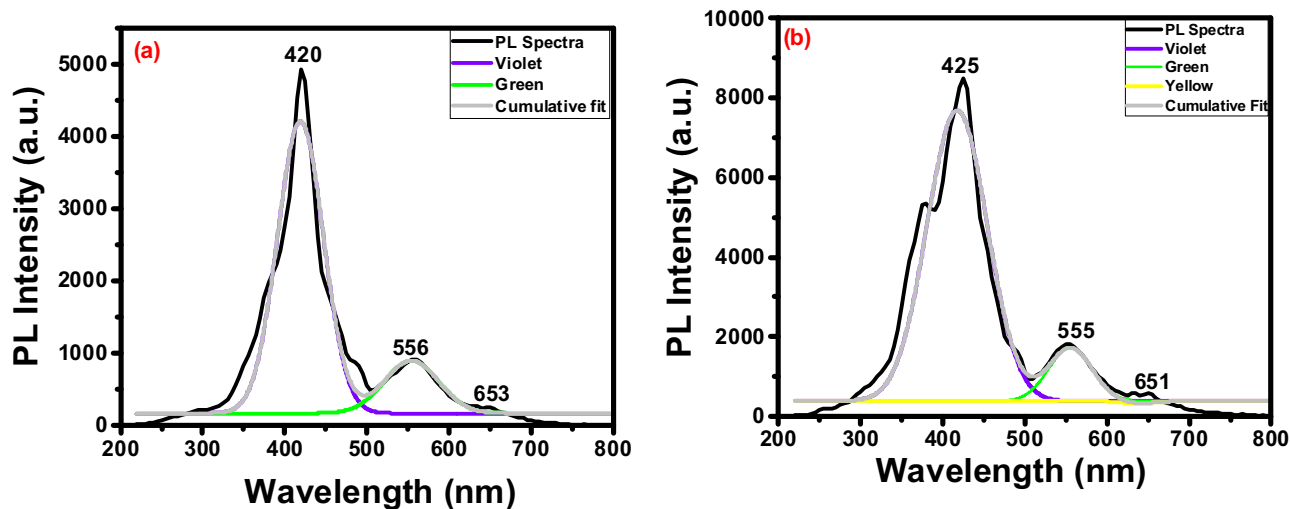


Fig. 7 Photoluminescence spectra of the synthesized (a) $\text{GO/ZnO}_{0.6}\text{NiO}_{0.4}$ and (b) $\text{GO/ZnO}_{0.4}\text{NiO}_{0.6}$ materials

ZnO in the composite decreases, the number of PL peaks and intensity reduces. The three labeled PL peaks observed correspond to approximately 3.0 eV, 2.2 eV, and 1.9 eV energy values respectively. A deconvolution of the humps confirmed the presence of other absorption edges which could be due to the presence of more than one energy band gap value in the spectra [40].

3.6 FTIR analysis

Figure 8 shows the FTIR spectra of the $\text{GO/ZnO}_{0.4}\text{NiO}_{0.6}$ and $\text{GO/ZnO}_{0.6}\text{NiO}_{0.4}$ ternary nanocomposites in the range of 0 to 4000 cm^{-1} . The absorption peaks around 554, 670, 1220, 1357, 1622, 1721, 2833, 2849, and 2929 cm^{-1} correspond to following functional group C-Cl (strong), C=S (strong), carbon-carbon double bonds (C=C), Ketone (moderate), OH (weak), and CH=CH (strong) respectively. Other peaks include absorption peaks at 3443 cm^{-1} and 3411 cm^{-1} representing the hydroxyl groups also belonging to the GO. The distinctive bands at 554 to 1040 cm^{-1} could be attributed to the stretching vibration of the metal oxides, in this case, due to NiO or ZnO metal group, suggesting the successful synthesis of the composites. These spectra revealed characteristic peaks between 426 and 670 cm^{-1} which correspond to Zn-O and Ni-O vibrational stretching modes. It can be noticed that the intensities and stretching vibrations of the ternary composites are higher at higher volume ratios of the NiO constituent [41]. These results confirm that the ternary composite is successfully synthesized. It can also be observed that as the volume of ZnO increases, the number of bands increases. The band shifts observed could be attributed to the volume ratio of ZnO and NiO; hence, ascertaining that the volume ratio is responsible [42].

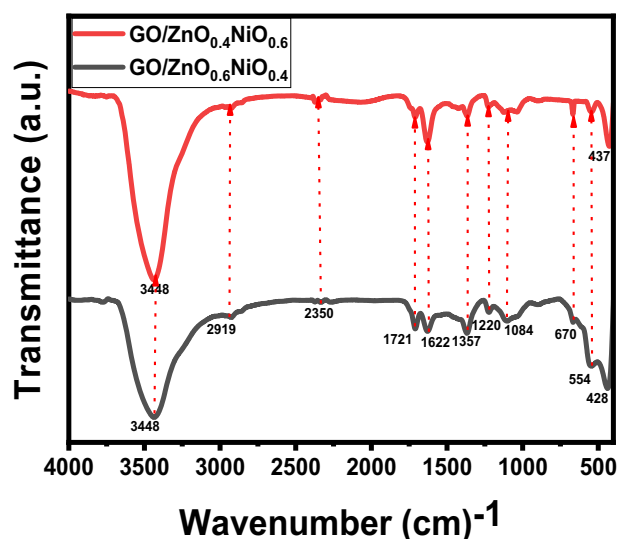


Fig. 8 FTIR spectra of the synthesized $\text{GO/ZnO}_{0.4}\text{NiO}_{0.6}$ and $\text{GO/ZnO}_{0.6}\text{NiO}_{0.4}$ composites

3.7 Gas sensing measurements

3.7.1 Thermal conductivity study

Figure 9a, b give the relationship between the current versus voltage and current versus operating temperature for the synthesized $\text{GO/ZnO}_{0.4}\text{NiO}_{0.6}$ and $\text{GO/ZnO}_{0.6}\text{NiO}_{0.4}$ ternary nano composites obtained at 100 ppm and an applied potential of 10 V. The composite having a higher volume ratio of the zinc oxide constituent recorded slightly higher increase in current. This corresponds to the lower energy band gap of the higher zinc oxide-containing composite as compared to that of the nickel oxide. The thermal conductivity curves showed a similar pattern for both the $\text{GO/ZnO}_{0.6}\text{NiO}_{0.4}$ and $\text{GO/ZnO}_{0.4}\text{NiO}_{0.6}$ samples and were taken from 50 to

400 °C operating temperature. The plots show a steady flow of as the operating temperature increased to 325 °C for both composites. Above 325 °C, the ternary composites exhibited high conductivity which could be due to the synergy during the synthesis process and led to increasing current flow [43]. The linear nature of the plots suggests that the nanocomposites exhibit ohmic characteristics [44].

3.7.2 Gas response test

Figure 10a, b shows the gas response versus operating temperature for the GO/ZnO_{0.6}NiO_{0.4} and GO/ZnO_{0.4}NiO_{0.6} ternary nanocomposites obtained at 100 ppm and 10 V. The responses exhibited by the gases are unique and distinctive. The composites showed the highest response to chlorine gas Cl₂ at an operating temperature of 300 °C while their highest response to ethanol was recorded at 400 °C. The gas responses are seen to increase as the operating temperature increases from 100 to 400 °C. At 50 °C near room temperature, the samples exhibited an upward shift in their response to chlorine gas. This sudden increase in the gas response as compared to the 100 and 150 °C temperatures may be attributed to the lower energy values obtained from the photoluminescence spectra at higher values [45]. The differential in the gas responses over a range of operating temperatures shows the effect of variational volume ratios. As the volume of ZnO increases in the nano composite; the sensitivity to ethanol and chlorine gas increases due to the relative lower energy band gap of ZnO as compared to NiO [46–48]. This increase could also be due to large crystallite size of GO/ZnO_{0.6}NiO_{0.4} as related to GO/ZnO_{0.4}NiO_{0.6}. Overall, the composites showed higher response to chlorine gas as compared to ethanol.

3.8 Selectivity and gas concentration in ppm analysis

The relationships between their responses and the gases have been shown in Fig. 11a for the GO/ZnO_{0.6}NiO_{0.4}, and GO/ZnO_{0.4}NiO_{0.6} composites. The nano composites measured at 300 °C, 100 ppm, and 10 V were highly sensitive to chlorine (Cl₂) and less sensitive to ethanol. The graphs show a steady increase in the sensitivity at higher ZnO volume percentage. The high sensitivity exhibited by the nano composite could be linked to the synergy in the nano composite during the sol–gel synthesis process. The gas response relationship versus ppm has also been illustrated in Fig. 11b. The graph shows a steady increase in the gas response as the ppm increases until at about 150–ppm where the nano composites attained maximum gas response sensitivity. It can be observed that further increase in ppm caused no further increase in the sensitivity and this stability was maintained up until 420 ppm. This is because the electron at the surface of the composites got completely attached and no further increase in the ppm created any increase in the gaseous sensitivity of the nano composites [49].

3.9 Photocatalytic measurements

The photocatalytic activity measurement of GO/ZnO_{0.6}NiO_{0.4} and GO/ZnO_{0.4}NiO_{0.6} ternary nanocomposites measured at 80 W/m² and 10 ppm are illustrated in Fig. 12a, b. The efficiencies of the 10 mg nanoparticles used for the methylene blue degradation were 88.7 and 87.2% respectively. The GO/ZnO_{0.6}NiO_{0.4} composite recorded slightly higher degradation efficiency than the GO/ZnO_{0.4}NiO_{0.6} composite. The high absorbance features show that the nanocomposite materials are good photocatalytic materials [11, 24].

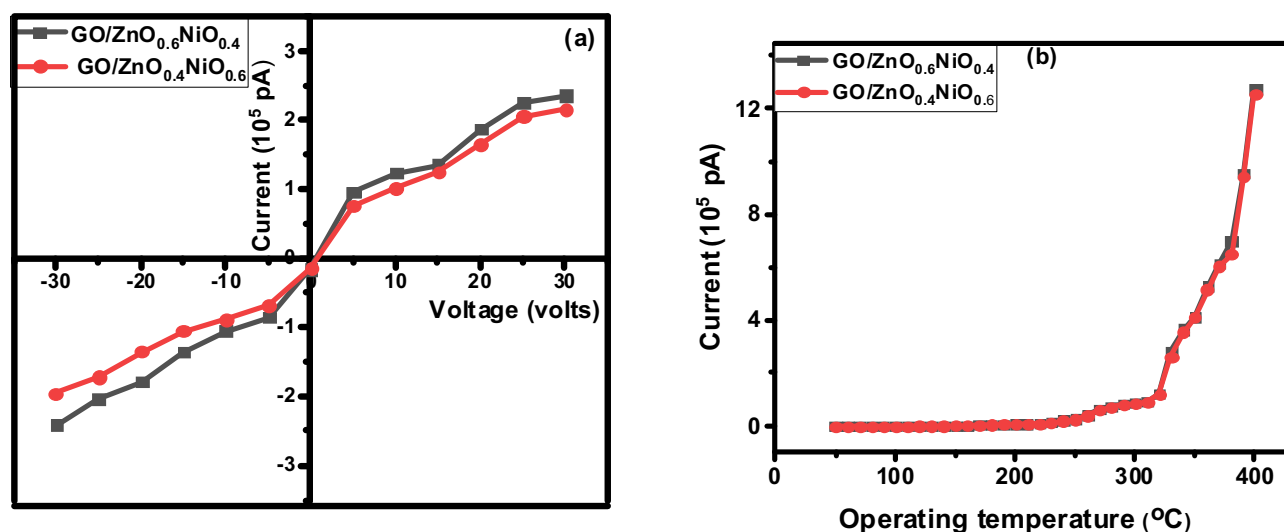


Fig. 9 a Current versus voltage and (b) current versus temperature plots of the ternary composites

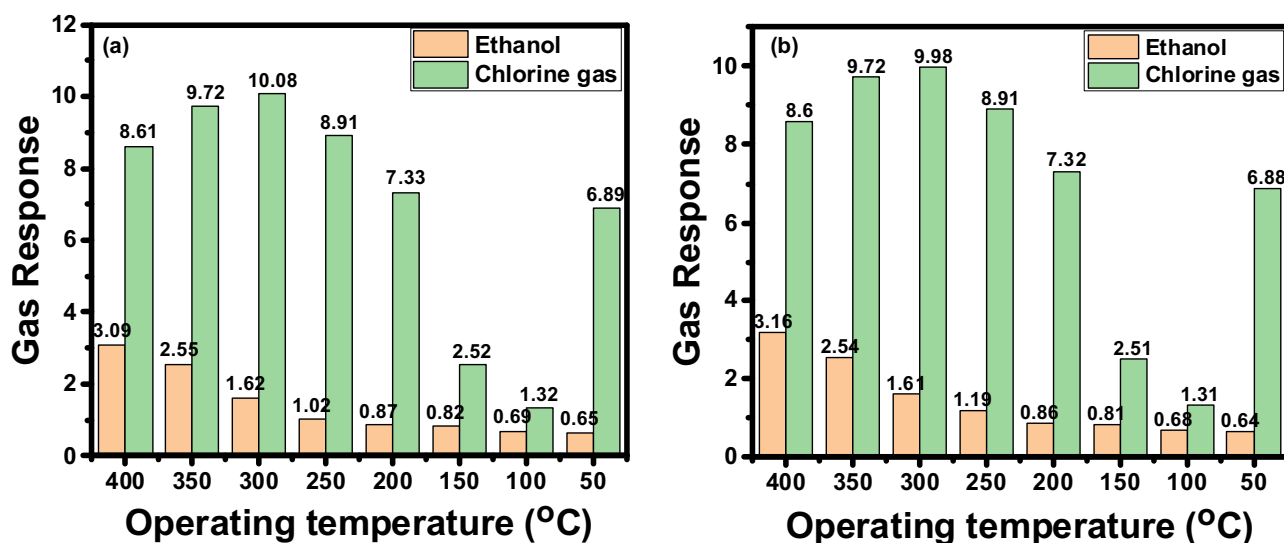


Fig. 10 Gas response versus temperature histograms of the (a) GO/ZnO_{0.6}NiO_{0.4} (b) GO/ZnO_{0.4}NiO_{0.6} ternary composites

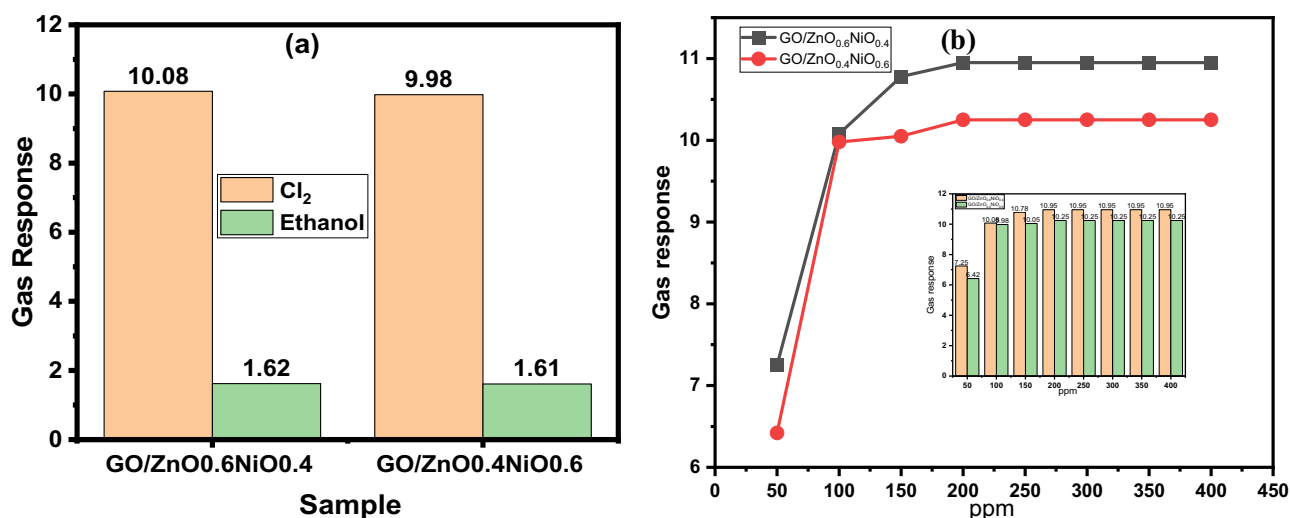


Fig. 11 Plots showing the (a) Gas selectivity plot (b) Gas concentration plot of the synthesized samples' gas response versus ppm for the synthesized composites

The reaction rate equation $\ln(C_0/C_t) = Kt$ gives the relationship between $\ln(C_0/C_t)$ and the exposing time t from which the pseudo-first order rate constant, K was determined [50]. From the equation; C_0 is the concentration at an exposing time of zero while C_t is the concentration at an exposing time t . The graph of this relation is illustrated in Fig. 13a while Fig. 13b is the fitted first order graph. The slope of the graph represents the pseudo-first order rate constant (K) with obtained values for the GOZnO_{0.6}NiO_{0.4} and GOZnO_{0.4}NiO_{0.6} ternary composites as 0.022 per min and 0.023 per min respectively. The pseudo-first order rate constant increased as the volume of ZnO increased in the nano composite. This shows that the volume ratio affects the pseudo-first order rate constant. Table 1 describes the several parameters of pseudo-first order rate constant, K . The degradation efficiency

obtained at different degradation times was also calculated. The synthesized ternary composite was highly effective in dye degradation with efficiency of over 85% respectively obtained over time for the pseudo-first order rate constant [51, 52].

4 Conclusions

Ternary composites of GOZnO_{0.6}NiO_{0.4} and GOZnO_{0.4}NiO_{0.6} were synthesized by a sol-gel technique using reflux reaction. The deposited ternary nano composites were characterized for their structural, morphological, elemental, optical, photoluminescent, conductive, gas sensing, and photocatalytic properties. XRD results showed prominent peaks with cubic and hexagonal crystal structures revealed. The micrographs

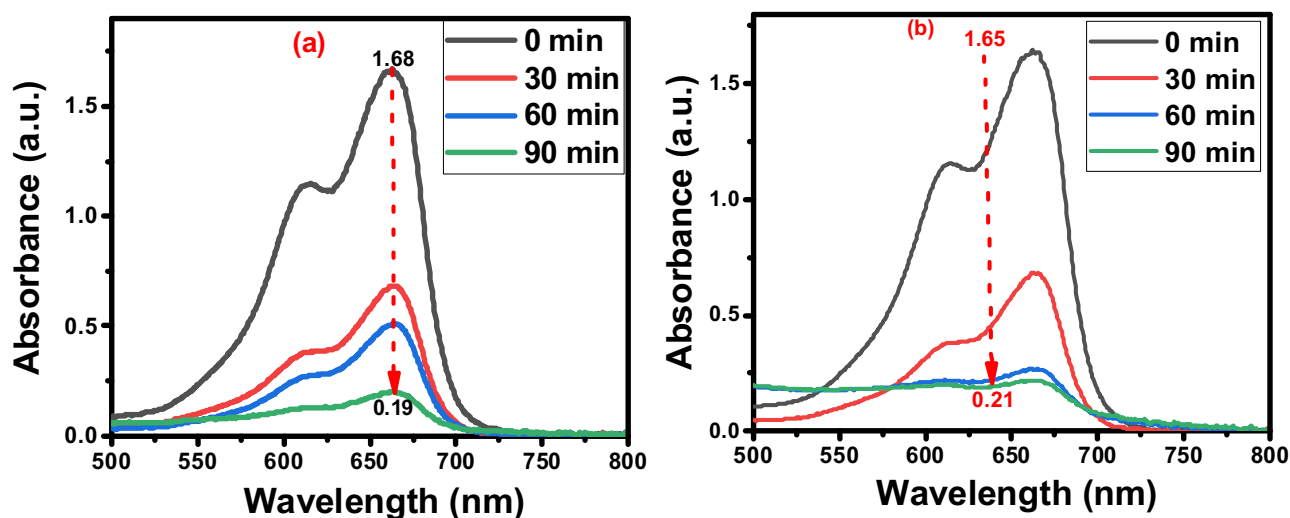


Fig. 12 Plots showing the photocatalytic responses of the measured (a) $\text{GO/ZnO}_{0.6}\text{NiO}_{0.4}$ and (b) $\text{GO/ZnO}_{0.4}\text{NiO}_{0.6}$ composites

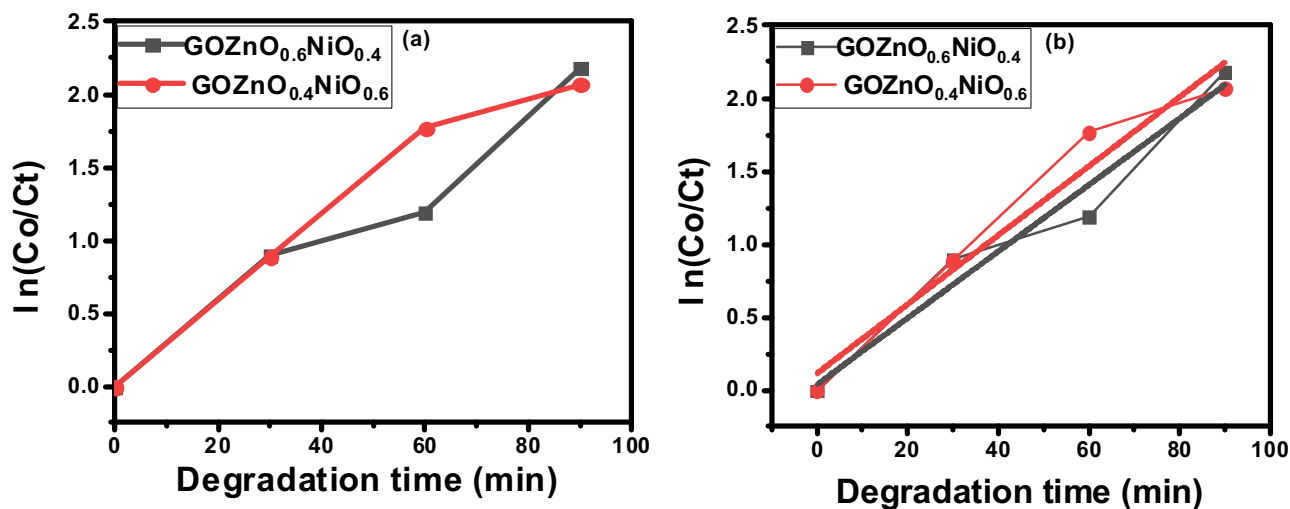


Fig. 13 Plots showing the (a) pseudo-first order plot and (b) fitted pseudo-first order plot for the synthesized samples

Table 1 Degradation parameters for the (a) $\text{GO/ZnO}_{0.6}\text{NiO}_{0.4}$ and (b) $\text{GO/ZnO}_{0.4}\text{NiO}_{0.6}$ composites

Time (min)	a				b			
	Ct	Co/Ct	$\ln(\text{Co/Ct})$	Degradation eff. (%)	Ct	Co/Ct	$\ln(\text{Co/Ct})$	Degradation eff. (%)
0	1.68	1.00	0.00	0.0	1.65	1.00	0.00	0.0
30	0.68	2.47	0.90	59.5	0.68	2.43	0.89	58.7
60	0.51	3.29	1.19	69.6	0.28	5.89	1.77	83.0
90	0.19	8.84	2.18	88.7	0.21	7.89	2.07	87.2

showed dense nano web-like morphology distributed over the surface. The EDS results revealed the presence of all the basic elements in the ternary nanocomposite with their corresponding percentages attached as insets. The optical plots gave high absorbance features in the ultraviolet region with energy band gaps ranging from 3.0 to 3.4 eV gotten from the Tauc's plots. The PL spectra showed different emission peaks with energy

values varying from 1.9 to 3 eV at different wavelength regions. The different functional groups and vibrational modes present in the ternary composites were revealed in the FTOR spectra. The composites exhibit higher gas sensing capacity to chlorine gas as compared to the ethanol. High thermal conductivity and good photocatalytic activity of the synthesized samples have been shown from the characterization. These

variations in the obtained results could be linked to the variations in the volume ratio of ZnO and NiO. The fabricated composites exhibited qualities that are potentially useful in gas sensing and photocatalytic devices.

Acknowledgements The authors are thankful to DST, New Delhi for providing Research Infrastructure under the DST-FIST Scheme. This work was supported by the Deanship of Scientific Research, Vice Presidency for Graduate Studies and Scientific Research, King Faisal University, Saudi Arabia [Grant No. KF241009].

Author contributions Matthew, DF carried out the research investigation. Nkele AC took the correspondence, drafted and revised the manuscript. Patil, GE; Shinde, SD; Jain, GH; Nwakanma MO; Abhinay, SM supported the experimentation and characterization processes. Adil Alshoaibi supported the project with some funds from King Faisal University. Ezekoye, BA; Ekwealor, ABC; Ezema, FI supervised the project.

Compliance with ethical standards

Conflict of interest The authors declare no competing interests.

References

- Saber NB, Mezni A, Alrooqi A, Altalhi T (2020) A review of ternary nanostructures based noble metal/semiconductor for environmental and renewable energy applications. *Journal of Materials Research and Technology* 9:15233–15262. <https://doi.org/10.1016/j.jmrt.2020.10.090>
- Stobinski L, Lesiak B, Malolepszy A et al. (2014) Graphene oxide and reduced graphene oxide studied by the XRD, TEM and electron spectroscopy methods. *Journal of Electron Spectroscopy and Related Phenomena* 195:145–154. <https://doi.org/10.1016/j.elspec.2014.07.003>
- Nwankwo MC, Ezealigo B, Nwanya AC et al. (2020) Syntheses and characterizations of GO/Mn₃O₄ nanocomposite film electrode materials for supercapacitor applications. *Inorganic Chemistry Communications* 119:107983. <https://doi.org/10.1016/j.inoche.2020.107983>
- Azizighannad S, Mitra S (2018) Stepwise reduction of graphene oxide (GO) and its effects on chemical and colloidal properties. *Sci Rep* 8:1–8. <https://doi.org/10.1038/s41598-018-28353-6>
- Aljaafari A, Parveen N, Ahmad F et al. (2019) Self-assembled cube-like copper oxide derived from a metal-organic framework as a high-performance electrochemical supercapacitive electrode material. *Scientific Reports* 9:9140. <https://doi.org/10.1038/s41598-019-45557-6>
- Femi MD, More MA, Nkele AC et al. (2024) Sol-gel processed (Zn_xNi_{1-x})O binary composite characterized for gas sensing and photocatalytic applications. *J Mater Sci Mater Electron* 35:1300. <https://doi.org/10.1007/s10854-024-12936-3>
- Ansari SA, Yadav H, Adeel M et al. (2019) Solvothermal growth of 3D flower-like CoS@ FTO as high-performance counter electrode for dye-sensitized solar cell. *Journal of Materials Science Materials in Electronics* 30:6929–6935. <https://doi.org/10.1007/s10854-019-01008-6>
- Sawant SY, Kim JY, Han TH et al. (2018) Electrochemically active biofilm-assisted biogenic synthesis of an Ag-decorated ZnO@ C core-shell ternary plasmonic photocatalyst with enhanced visible-photocatalytic activity. *New Journal of Chemistry* 42:1995–2005. <https://doi.org/10.1039/C7NJ03936K>
- Ansari SA, Cho MH (2017) Simple and large scale construction of MoS₂-g-C₃N₄ heterostructures using mechanochemistry for high performance electrochemical supercapacitor and visible light photocatalytic applications. *Scientific reports* 7:43055. <https://doi.org/10.1038/srep43055>
- Cortie MB, McDonagh AM (2011) Synthesis and optical properties of hybrid and alloy plasmonic nanoparticles. *Chemical reviews* 111:3713–3735. <https://doi.org/10.1021/cr1002529>
- Munawar T, Iqbal F, Yasmeen S et al. (2020) Multi metal oxide NiO-CdO-ZnO nanocomposite-synthesis, structural, optical, electrical properties and enhanced sunlight driven photocatalytic activity. *Ceramics International* 46:2421–2437. <https://doi.org/10.1016/j.ceramint.2019.09.236>
- Pal K, Chakroborty S, Nath N (2022) Limitations of nanomaterials insights in green chemistry sustainable route: Review on novel applications. *Green Processing and Synthesis* 11:951–964. <https://doi.org/10.1515/gps-2022-0081>
- Yuan C, Wu HB, Xie Y, Lou XW (2014) Mixed transition-metal oxides: design, synthesis, and energy-related applications. *Angewandte Chemie International Edition* 53:1488–1504. <https://doi.org/10.1002/anie.201303971>
- Benrezgua E, Deghfel B, Zoukel A et al. (2022) Synthesis and properties of copper doped zinc oxide thin films by sol-gel, spin coating and dipping: a characterization review. *Journal of Molecular Structure* 1267:133639. <https://doi.org/10.1016/j.molstruc.2022.133639>
- Li S, Cai J, Wu X et al. (2018) TiO₂@ Pt@ CeO₂ nanocomposite as a bifunctional catalyst for enhancing photo-reduction of Cr (VI) and photo-oxidation of benzyl alcohol. *Journal of Hazardous Materials* 346:52–61. <https://doi.org/10.1016/j.jhazmat.2017.12.001>
- Wang Y, Van de Vyver S, Sharma KK, Román-Leshkov Y (2014) Insights into the stability of gold nanoparticles supported on metal oxides for the base-free oxidation of glucose to gluconic acid. *Green Chemistry* 16:719–726. <https://doi.org/10.10139/C3GC41362D>
- Tang P, Livraghi S, Giamello E et al. (2021) Ce doping boosts the thermo-and photocatalytic oxidation of CO at low temperature in TiZrO₄ solid solutions. *Advanced Materials Interfaces* 8:2100532. <https://doi.org/10.1002/admi.202100532>
- Nkele AC, Ezema FI, Nkele AC, Ezema FI (2020) Diverse synthesis and characterization techniques of nanoparticles. *IntechOpen*. <https://doi.org/10.5772/intechopen.94453>
- Teoh LG, Li K-D (2012) Synthesis and characterization of NiO nanoparticles by sol-gel method. *Materials Transactions* 53:2135–2140. <https://doi.org/10.2320/matertrans.M2012244>
- Jastrzębska AM, Jureczko J, Karcz J et al. (2017) Controlled synthesis of graphene oxide/alumina nanocomposites using a new dry sol-gel method of synthesis. *Chem Pap* 71:579–595. <https://doi.org/10.1007/s11696-016-0040-4>
- Nkele AC, Chime CP, Ezema FI (2022) Recent advances in graphene oxide-based fuel cells. CRC Press. eBook ISBN 9781003215196
- Nkele AC, Chime CP, Ezema FI (2023) Advances in fabricating Mn₃O₄ and its carbon composite for electrochemical energy storage applications. In: *Chemically deposited metal chalcogenide-based carbon composites for versatile applications*. Springer, p 179–192. https://doi.org/10.1007/978-3-031-23401-9_6
- Hintze C, Morita K, Riedel R et al. (2016) Facile sol-gel synthesis of reduced graphene oxide/silica nanocomposites. *Journal of the European Ceramic Society* 36:2923–2930. <https://doi.org/10.1016/j.jeurceramsoc.2015.11.033>
- Velasco-Hernández A, Esparza-Muñoz RA, de Moure-Flores FJ et al. (2020) Synthesis and characterization of graphene oxide - TiO₂ thin films by sol-gel for photocatalytic applications. *Materials Science in Semiconductor Processing* 114:105082. <https://doi.org/10.1016/j.mssp.2020.105082>

25. Lim MB, Hu M, Manandhar S et al. (2015) Ultrafast sol–gel synthesis of graphene aerogel materials. *Carbon* 95:616–624. <https://doi.org/10.1016/j.carbon.2015.08.037>
26. Jang J-H, Oh B, Lee E-J (2021) Crystalline hydroxyapatite/graphene oxide complex by low-temperature sol–gel synthesis and its characterization. *Ceramics International* 47:27677–27684. <https://doi.org/10.1016/j.ceramint.2021.06.192>
27. Nkele AC, Ezugwu S, Suguyima M, Ezema FI (2021) Structural and Electronic Properties of Metal Oxides and Their Applications in Solar Cells. In: Ezema FI, Lokhande CD, Jose R (eds) *Chemically Deposited Nanocrystalline Metal Oxide Thin Films: Synthesis, Characterizations, and Applications*. Springer International Publishing, Cham, p 147–163. https://doi.org/10.1007/978-3-030-68462-4_6
28. Nkele AC, Chime UK, Nwanya AC et al. (2019) Role of metallic dopants on the properties of copper (I) iodide nanopod-like structures. *Vacuum* 161:306–313. <https://doi.org/10.1016/j.vacuum.2018.12.049>
29. Ighodalo KO, Obi D, Agbogu A et al. (2017) The structural and optical properties of metallic doped copper (I) iodide thin films synthesized by SILAR method. *Materials Research Bulletin* 94:528–536. <https://doi.org/10.1016/j.materresbull.2017.06.032>
30. Nkele AC, Nwanya AC, Nwankwo NU et al. (2019) Structural, optical and electrochemical properties of SILAR-deposited zirconium-doped cadmium oxide thin films. *Mater Res Express* 6:096439. <https://doi.org/10.1088/2053-1591/ab31f5>
31. Çayır Taşdemirci T (2019) Influence of annealing on properties of SILAR deposited nickel oxide films. *Vacuum* 167:189–194. <https://doi.org/10.1016/j.vacuum.2019.05.047>
32. Zahid Ishaque M, Zaman Y, Arif A et al. (2023) Fabrication of ternary metal oxide (ZnO:NiO:CuO) nanocomposite heterojunctions for enhanced photocatalytic and antibacterial applications. *RSC Advances* 13:30838–30854. <https://doi.org/10.1039/D3RA05170F>
33. Handayani M, Mulyaningsih Y, Aulia Anggoro M et al. (2022) One-pot synthesis of reduced graphene oxide/chitosan/zinc oxide ternary nanocomposites for supercapacitor electrodes with enhanced electrochemical properties. *Materials Letters* 314:131846. <https://doi.org/10.1016/j.matlet.2022.131846>
34. Selim MS, El-Safty SA, Abbas MA, Shenashen MA (2021) Facile design of graphene oxide-ZnO nanorod-based ternary nanocomposite as a superhydrophobic and corrosion-barrier coating. *Colloids and Surfaces A Physicochemical and Engineering Aspects* 611:125793. <https://doi.org/10.1016/j.colsurfa.2020.125793>
35. Altin I, Ma X, Boffa V et al. (2021) Hydrothermal preparation of B–TiO₂-graphene oxide ternary nanocomposite, characterization and photocatalytic degradation of bisphenol A under simulated solar irradiation. *Materials Science in Semiconductor Processing* 123:105591. <https://doi.org/10.1016/j.mssp.2020.105591>
36. Agobi AU, Ekpunobi AJ, Ikeuba AI, Louis H (2022) The effects of graphene oxide load on the optical, structural and electrical properties of ternary nanocomposites (Polyvinyl alcohol/copper/graphene oxide) for electronic and photovoltaic application. *Results in Optics* 8:100261. <https://doi.org/10.1016/j.rio.2022.100261>
37. Tsai M-S, Su P-G, Lu C-J (2020) Fabrication of a highly sensitive flexible humidity sensor based on Pt/polythiophene/reduced graphene oxide ternary nanocomposite films using a simple one-pot method. *Sensors and Actuators B Chemical* 324:128728. <https://doi.org/10.1016/j.snb.2020.128728>
38. Wang C, Yang Y, Li R et al. (2020) Polyaniline functionalized reduced graphene oxide/carbon nanotube ternary nanocomposite as a supercapacitor electrode. *Chem Commun* 56:4003–4006. <https://doi.org/10.1039/D0CC01028F>
39. Abdulhusain ZH, Alshamsi HA, Salavati-Niasari M (2022) Silver and zinc oxide decorated on reduced graphene oxide: Simple synthesis of a ternary heterojunction nanocomposite as an effective visible-active photocatalyst. *International Journal of Hydrogen Energy* 47:34036–34047. <https://doi.org/10.1016/j.ijhydene.2022.08.018>
40. Martins VHN, Siqueira NMS, Fonsaca JES et al. (2021) Ternary Nanocomposites of Reduced Graphene Oxide, Polyaniline, and Iron Oxide Applied for Energy Storage. *ACS Appl Nano Mater* 4:5553–5563. <https://doi.org/10.1021/acsanm.1c01036>
41. del Valle Pacciaroni A, Sosa VE (2009) Spectrometry: infrared spectra. In: *Isolation, identification and characterization of allelochemicals/natural products*. CRC Press, p 293–332. eBook ISBN 9780367803636.
42. Afifi M, Ahmed MK, Ibrahim HA et al. (2022) Improvement of physicochemical properties of ternary nanocomposites based on hydroxyapatite/CuO/graphene oxide for biomedical usages. *Ceramics International* 48:3993–4004. <https://doi.org/10.1016/j.ceramint.2021.10.186>
43. Khalilpourazary S, Meshkat SS, Salehi J (2021) Application of alumina/graphene nanocomposite to enhance the surface quality of Al7175-T74 specimens. *AUT Journal of Mechanical Engineering* 5:255–264. <https://doi.org/10.22060/ajme.2020.17420.5861>
44. Wu Y, Shu R, Zhang J et al. (2020) Oxygen vacancies regulated microwave absorption properties of reduced graphene oxide/multi-walled carbon nanotubes/cerium oxide ternary nanocomposite. *Journal of Alloys and Compounds* 819:152944. <https://doi.org/10.1016/j.jallcom.2019.152944>
45. Gandhi AC, Wu SY (2017) Strong deep-level-emission photoluminescence in NiO nanoparticles. *Nanomaterials* 7:231
46. Apeh OO, Chime UK, Agbo S et al. (2019) Properties of nanostructured ZnO thin films synthesized using a modified aqueous chemical growth method. *Mater Res Express* 6:056406. <https://doi.org/10.1088/2053-1591/aadcd6>
47. Nkele AC, Nwanya AC, Shinde NM et al. (2020) The use of nickel oxide as a hole transport material in perovskite solar cell configuration: Achieving a high performance and stable device. *International Journal of Energy Research* 44:9839–9863. <https://doi.org/10.1002/er.5563>
48. Nkele AC, Nwanya AC, Nwankwo NU et al. (2019) Investigating the properties of nano nest-like nickel oxide and the NiO/Perovskite for potential application as a hole transport material. *Adv Nat Sci Nanosci Nanotechnol* 10:045009. <https://doi.org/10.1088/2043-6254/ab5102>
49. AbdelHamid AA, Yang X, Yang J et al. (2016) Graphene-wrapped nickel sulfide nanoprisms with improved performance for Li-ion battery anodes and supercapacitors. *Nano Energy* 26:425–437. <https://doi.org/10.1016/j.nanoen.2016.05.046>
50. Ali SM, Dakhil OA, Hussein EH (2021) Modified hydrothermal preparation of ZnO/NiO nano-heterojunction for enhancement of photocatalytic activity. *Acta Physica Polonica A* 140. <https://doi.org/10.12693/APhysPo1A.140.327>
51. Moiz MA, Mumtaz A, Salman M et al. (2021) Enhancement of dye degradation by zinc oxide via transition-metal doping: a review. *J Electron Mater* 50:5106–5121. <https://doi.org/10.1007/s11664-021-09093-2>
52. Tatarchuk T, Danyliuk N, Shychuk A et al. (2021) Photocatalytic degradation of dyes using rutile TiO₂ synthesized by reverse micelle and low temperature methods: real-time monitoring of the degradation kinetics. *Journal of Molecular Liquids* 342:117407. <https://doi.org/10.1016/j.molliq.2021.117407>

Publisher's note Springer Nature remains neutral with regard to jurisdictional claims in published maps and institutional affiliations.

Springer Nature or its licensor (e.g. a society or other partner) holds exclusive rights to this article under a publishing agreement with the author(s) or other rightsholder(s); author self-archiving of the accepted manuscript version of this article is solely governed by the terms of such publishing agreement and applicable law.